Analysis of Wall Loss Currents in an ECR Magnetic Nozzle Thruster

Ari J. Eckhaus* and Benjamin A. Jorns†
University of Michigan, Ann Arbor, Mi, 48105

The plasma loss currents through the walls of a low-power electron cyclotron resonance magnetic nozzle thruster are experimentally characterized. A test article is employed where the walls of the plasma chamber have been isolated from the surrounding thruster body and the device is tested in two configurations. The first has the two surfaces isolated, where the floating potential of each is characterized independently. The second configuration connects the thruster body and wall through a shunt resistor, enabling direct measurements of the current flow. It is found that nearly 15% of the input power is lost to driving these wall currents. As a result, the connected configuration yields thrust values approximately 20% lower than the isolated case. This difference in performance is primarily attributed to a decrease in ion current resulting from plasma losses to the wall. As a secondary method of eliminating loss current pathways, a dielectric plate is added to the exit plane of the thruster. This addition improves performance of the device compared to the two other configurations tested. Total efficiency is increased from 4% in the connected configuration to 10% when the dielectric plate is added. The plate also eliminates dependence on the electrical configuration of the internal thruster components and reduces the current measured between the body and wall by an order of magnitude. These results are discussed in the context of non-local loss currents that form at the boundaries between the plasma and thruster surfaces. Thin sheath theory is applied to quantify these losses and compare the theoretical values to those observed experimentally.

I. Introduction

Over the past decade, research interest in low-power magnetic nozzle thrusters has steadily increased [1–5]. This family of electric propulsion (EP) systems has several potential benefits, including the ability to operate without an external electron source and compatibility with alternative propellants [5, 6]. Despite their promise, the performance of these magnetic nozzle thrusters has historically been too low for application to flight systems. However, in 2022, an electron cyclotron resonance (ECR) magnetic nozzle thruster achieved efficiencies in excess of 40% when operating at 30 W input power [7]. This groundbreaking result exceeds the performance of other, high TRL, EP devices in this power class and demonstrates the possibility for low-power magnetic nozzle thrusters to deliver on their promise.

Unfortunately, much of the work enabling this breakthrough focused on heuristic optimization of global performance metrics. Although this approach resulted in a single test article with competitive efficiency, the physical mechanisms by which performance improved were not fully reported. As a result, replication of this performance by other research groups and its extension to alternative propellants has not yet been achieved. Therefore, to continue building upon the potential of the low-power ECR magnetic nozzle architecture, it is necessary to understand and explain the experimentally-derived design decisions.

One notable result of previous ECR thruster research is a strong relationship between performance of the device and the materials used on thruster surfaces. This dependence was first observed when the metallic walls of the ECR discharge chamber were coated with an insulating layer of polyimide film [8]. Later studies compared wall materials made of aluminum, graphite, boron nitride and aluminum oxide [9, 10]. In each of these experiments, electrically insulating wall materials yielded higher performance than conductive materials. There is also evidence that this relationship between thruster performance and material conductivity extends beyond the walls of the plasma discharge region. Similar benefits have been suggested when electrically isolating the thruster plume from surfaces in the near-field region, including the thruster body, plates positioned near the thruster exit plane, and even the walls of the vacuum facility [9, 11–13].

The performance benefits observed when isolating components of the thruster is suspected to relate to formation of loss currents inside the thruster source region, or in the near-field of the plume. Indeed, current losses to the walls of the

---

*PhD Candidate, Aerospace Engineering, aeckhaus@umich.edu

†Associate Professor, Aerospace Engineering, AIAA Associate Fellow.

plasma chamber can represent performance-limiting loss mechanisms for other EP systems and therefore require unique design considerations [14]. In ECR thrusters, these loss currents are particularly costly, as the lack of electron source means that each free electron must be generated through ionization. Loss currents of these electrons therefore inhibit ionization. In this way, electron currents to the walls of the device have been suggested to cause lower ion currents in the plume, corresponding to a reduction in thrust.[11]. Although this hypothesis does explain the observed performance trends, these wall currents have yet to be fully characterized experimentally.

In this paper, we perform a detailed investigation of the dependence between device performance and conductivity of the surfaces in the plume. We utilize a test article that allows us to measure the current flowing between the thruster body and plasma source region and determine how this current changes when a dielectric plate is added to the exit plane of the thruster. This work is organized in the following way. First, in Sec.II, we describe the principle of operation of ECR magnetic nozzle thrusters and elaborate on the effects of wall currents. In Sec. III, we then detail our experimental apparatus, including the thruster, vacuum facility, and diagnostics used. In Sec. IV, we present the results of our study including global performance measurements and efficiency mode analysis for each thruster configuration studied. We then physically interpret these results using thin sheath theory in Sec. V. Finally, we present concluding remarks about the role of wall conductivity and loss currents in Sec. VI.

II. ECR Thruster Principle of Operation

In this section we further motivate our investigation of wall currents in ECR thrusters. We begin by describing the principle of operation for the low-power, coaxial device used in this work. We then briefly discuss the theoretical effects of loss currents to the walls of the thruster.

A. Coaxial ECR Thruster with Magnetic Nozzle

Operation of ECR magnetic nozzle thrusters relies on conversion of electron thermal energy into directed ion kinetic energy. This energy conversion is accomplished in two stages: a plasma source region and a magnetic nozzle. These sections of the thruster are highlighted in Fig. 1. In the plasma source region, microwave energy is resonantly coupled into the electrons of a plasma. This ECR interaction efficiently heats the electrons, which then ionize injected neutral propellant to maintain the plasma discharge. In this part of the thruster, the magnetic field is nearly axial, confining electrons away from the walls of the device. However, electrons are highly mobile along magnetic field lines, allowing them to stream away from the source region. As the electrons exit the plasma source, the heavy, unheated, ions remain. This charge imbalance induces an electric field, accelerating the ions downstream. Finally, as the magnetic nozzle expands, azimuthal currents are generated in the thruster plume. These currents oppose the applied magnetic field, resulting in a thrust force.

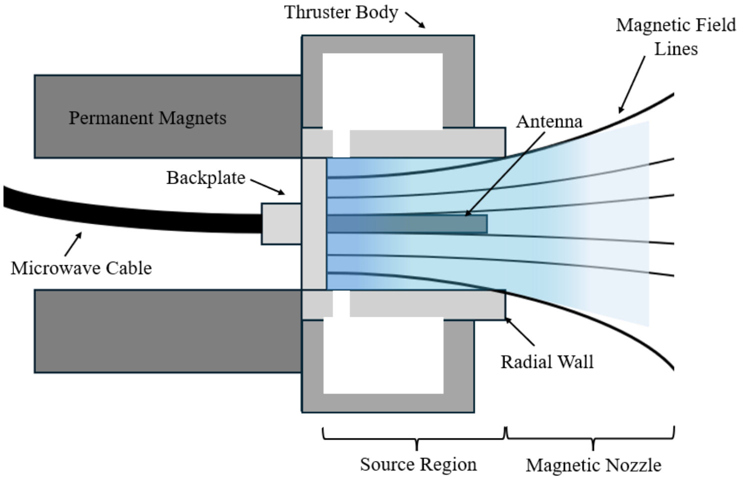

Fig. 1 Notional Geometry of a Coaxial ECR Magnetic Nozzle Thurster

Typically, low-power ECR magnetic nozzle thrusters adopt a coaxial power coupling scheme. The notional geometry of a coaxial device is shown in Fig. 1. Microwave energy is delivered through the central antenna and coupled into the plasma over a thin plane, the so called "resonance zone.” At this axial location the magnetic field strength is tuned to satisfy the ECR condition. The plasma discharge chamber is bound by an insulating back wall, commonly made of boron nitride, and a cylindrical radial wall. Neutral propellant is often injected through this radial wall after passing through a gas distribution plenum. The magnetic nozzle is established using a set of permanent magnets located behind the plasma source region.

B. Electrical Configuration and The Role of Wall Currents

During operation of the ECR thruster, the plasma discharge sustained in the source region is born with some inherent potential, ϕ_p. Because the walls of the device are directly in contact with the plasma, they too are exposed to an electrical potential. However, the disparity in electron and ion mobility causes the formation of a plasma sheath where the voltage at the walls is slightly negative compared to the plasma potential. This thin sheath serves to repel electrons and attract ions [14, 15]. In doing so, the sheath offsets the disparity in species mobility and maintains a zero-net current condition to the walls.

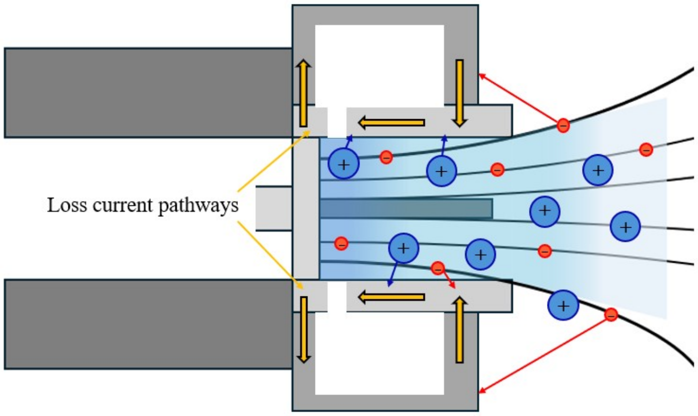

Fig. 2 Example of non-local currents between thruster body and plasma source

Although any electrically isolated object exposed to a plasma will collect zero-net current, if the surface is conducting, it is possible for local currents to form, which may be offset by currents of the opposite species elsewhere in the plasma. For example, in the source region of the ECR magnetic nozzle thruster, the strong axial magnetic field prevents diffusion of electrons radially towards the walls. However, the more massive ions are relatively unaffected by the magnetic field. This may create a scenario, like the one shown in Fig. 2, where an electron loss current to the external thruster body is offset by ion currents within the source region. In this case, the zero-net current condition remains satisfied, despite the fact that the ion and electron loss currents occur at different locations on the thruster. Indeed, provided as any thruster components are electrically connected, these non-local currents may form, and the zero-net current can be maintained. The presence of these non-local current loops may negatively impact the behavior of ECR magnetic nozzle thrusters, as well as other ECR ion sources [10–12, 16].

Several design strategies have been proposed to eliminate current loops from the discharge of ECR magnetic nozzle thrusters. One approach involves manufacturing the radial thruster walls from electrically insulating materials, potentially eliminating current pathways between the plasma source chamber and other parts of the device [10]. A second design includes a dielectric plate near the exit plane of the thruster [11, 12]. It is suggested that this dielectric plate blocks the back-streaming current of electrons, eliminating current loops through the thruster body. Although each of these designs have resulted in performance improvements, the hypothesis that these strategies effectively mitigate current loops in the thruster has yet to be confirmed. In this work we experimentally test multiple configurations of an ECR magnetic nozzle thruster and directly measure the current between various components. In this way we are able to evaluate the effectiveness of each design strategy in mitigating non-local currents in the plasma discharge.

III. Approach and Experimental Setup

In this section, we detail the experimental apparatus used to investigate loss currents through the walls of an ECR thruster. We begin with a description of the low-power ECR magnetic nozzle thruster tested. This is followed by discussion of the facility and diagnostic suite utilized. We then conclude with an overview of the efficiency mode analysis used to gain additional insight into thruster behavior.

A. ECR Thruster Test Article

The ECR magnetic nozzle test article we use in this work is the University of Michigan's (UM) ECR v.2 thruster. Similar to the low-power designs pioneered by the French Aerospace Lab, Office National d'Études et de Recherches Aérospatiales (ONERA), this device adopts the coaxial coupling scheme described in Sec. II. This family of ECR thrusters is designed to operate at a nominal power of 30 W and propellant flow rate of 1 SCCM-Xe. The UM ECR v.2 thruster is intended to be highly modular, allowing components to easily be exchanged for parts of different materials or geometries. Here, we equip the thruster with entirely aluminum components; both the source region walls and the surrounding thruster body are manufactured from aluminum 6061. We note that the use of an untreated aluminum thruster body is a departure from many of the previous characterizations performed for this test article [4, 10]. Although the anodization does not create a perfectly insulating material, the resulting oxide layer inhibits current collection on the thruster body. Based on the discussion in Sec. II.B, we do expect the anodization to improve thruster performance. However, for the purposes of experimentally investigating loss currents between various thruster components, we need these surfaces to be electrically conductive. As a result, in this study we use untreated aluminum for both the wall of the plasma source region and the thruster body.

1. Isolation of Thruster Components

In the configuration described above, both the thruster body and source region wall are manufactured of electrically conductive material. Under typical thruster assembly, the body and the source region would therefore be electrically connected. However, this bulk connection obscures our ability to measure current flowing between the two components. Instead, we electrically isolate the thruster body and source and introduce only a single current pathway that can be directly measured. To accomplish this, the surfaces of the plasma source region which contact the body are covered with a combination of mica sheets and Kapton polyimide film. Sense lines are then run from both the thruster body and source wall. Isolation between the two components is verified using a Megger BM25. During this study, the resistance between the thruster body and source wall is measured to be above 45 GΩ when a 500 V bias was applied.

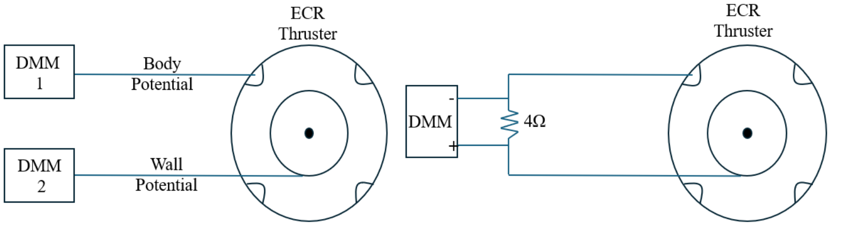

a) Isolated Configuration

b) Connected Configuration

Fig. 3 Comparison of Electrically a) Isolated and b) Connected thruster test configuraitons

The isolation scheme described above results in two test arrangements, each of which are shown in Fig. 3. In one case, the body and source wall are isolated and the floating potential of each part can be measured independently. In the second case, the sense lines of the body and source wall can be connected through a shunt resistor. It is desirable for the value of this shunt resistor to be low, to minimize the potential difference between the thruster source and body. In our experiments, we use a 4Ω shunt resistor to keep the voltage difference between the two components less than 1 V.

2. Addition of a Downstream Plate

Previous experiments have reported performance improvements when a dielectric plate is added near the exit plane of the thruster [11]. To test the impact of this plate on the wall loss currents within the thruster, we attach a dielectric plate to the thruster body. As shown in Fig. 4(b), the plate is a 15.25 cm square, made of aluminum oxide. A 3.8 cm diameter hole is drilled in the center to accommodate the exit of the source region. Mechanically, this plate is attached to the thruster body using four fasteners. To prevent any current leaks, the fasteners used for this experiment are made from PEEK high-temperature plastic. With the addition of the plate, we retain the ability to isolate the internal wall and thruster body, and the same two electrical configurations are tested when the plate is added.

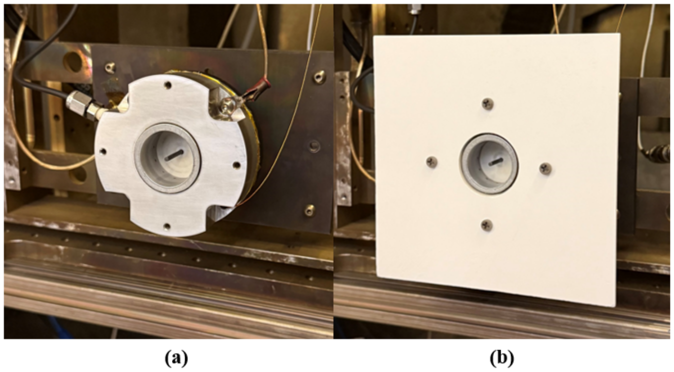

Fig. 4 (a) UM ECR V.II thruster with untreated aluminum source region wall and thruster body. (b) UM ECR V.II thruster with an aluminum oxide plate added to the thruster exit plane.

B. Vacuum Facility and Diagnostics

The vacuum chamber used in this work is the Junior Test Facility at the University of Michigan's Plasmadynamics and Electric Propulsion Laboratory (PEPL). Junior has a pumping speed of 40 kL/s on xenon and maintains a base pressure on the order of 5 μTorr-N$_2$. For low-power ECR testing, Junior has also been equipped with a pendulum-style, micro-Newton thrust stand [4]. This stand uses an optical displacement sensor to measure small deflections of the pendulum when the thruster is operating and has a resolution of approximately 13 μN. In addition to thrust, propellant flow, $\dot{m}$, is monitored using an Alicat 50-SCCM mass flow controller, and microwave power, P, is monitored using an Agilent N1912A power meter. These direct measurements of thrust, power, and propellant flow rate allow us to determine the global performance of the thruster, including thrust, specific impulse and total efficiency.

To gain insight into the behavior of the plasma, Junior is outfitted with a plasma diagnostic suite. As described in Ref. [10], this includes a Langmuir probe, Retarding Potential Analyzer (RPA), E×B probe, and Faraday probe. These probes are fixed to motion stages and placed in the far-field plume of the thruster. The E×B, Langmuir probe, and RPA measurements are taken on centerline at a distance of 50 cm downstream. The Faraday probe is swept angularly across the thruster centerline at a distance of 30 cm. The plasma properties measured by these probes provide additional information about the thruster operation and allow us to evaluate individual efficiency modes, each of which contribute to total efficiency. All data is processed according to the EP best practice for the respective probe [17–20]. We provide additional details about our far-field probe analysis in the appendix of this paper (Sec. VII).

C. Efficiency Mode Analysis

To relate changes in plasma properties to changes in global behavior of the thruster, we divide the total efficiency of the device into several efficiency modes. For ECR thrusters, it is common to use three efficiency modes: divergence efficiency, η_d, mass utilization efficiency, η_m, and energy efficiency, η_e [5, 8, 10–12]. These efficiencies are defined such that

$$\eta = \eta_D \eta_m \eta_e, \tag{1}$$

$$\eta_d = cos(\theta_D)^2, \tag{2}$$

$$\eta_m = \frac{I_i m_i}{q\dot{m}}, \tag{3}$$

$$\eta_e = \frac{E_i I_i}{P}. \tag{4}$$

$$\tag{5}$$

In the above expressions, θ_D represents the divergence half angle of the plume, I_i is the ion current emitted from the device, m_i is the mass of the ion species, q is the fundamental charge, and E_i is the mean ion energy. The physical properties of the plume required for this analysis are measured using the plasma diagnostic suite described in the previous section. The data collection and processing methods for each probe are described in detail in Sec. VII. This treatment of efficiency allows us to better understand the physical mechanisms that cause changes to global performance of the ECR thruster.

IV. Results

In this section we present the results of our experimental characterization of wall loss currents. We first present a comparison of thruster behavior when the walls of the thruster are electrically isolated and connected. This includes global metrics such as floating potential, wall current, and thrust, along with the efficiency mode analysis. We then repeat this comparison with the addition of the dielectric plate in the exit plane.

A. Comparison of Electrical Configuration

Here we present performance results for the thruster tested in the two electrical configurations shown in Fig. 3(b). We note that the experimental setup described in Sec. III allows the thruster configuration to be changed in situ, via a connection external to the vacuum chamber. Therefore, we are able to directly compare thruster behavior in an identical vacuum environment. For all data presented, the thruster is operated on xenon propellant with a flow rate of 1 SCCM and delivered power is varied from 20 W to 40 W in 5 W increments.

1. Floating Potential Comparison and Wall Current Measurements

We first compare the floating potential of the thruster components in the isolated and connected states. (Fig. 5 (a)).

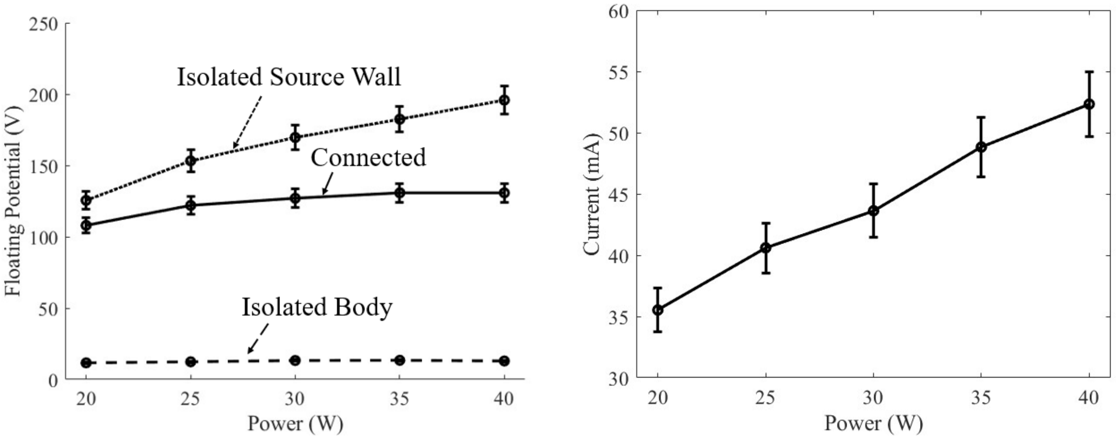

(a) (b)

Fig. 5 (a)Comparison of floating potentials of thruster components in the isolated and connected configurations. (b) Measured current between the thruster body and source as a function of delivered power

One immediate observation from these floating potential measurements is the comparatively low potentials observed on the thruster body in the isolated configuration. The isolated body voltage is approximately 10 V, compared to the 135 V-200 V potentials measured at the wall of the plasma source. We also see that, in the isolated configuration, potential on the thruster body is relatively unchanged by thruster operating power. This is contrasted by the potential at the source region wall, which monotonically increases across the power range tested. Physically, the increase in floating potential of the source wall is consistent with higher plasma potentials expected in the source region as more power is deposited into the plasma. This is indicative of increased electron temperatures in the source region as power increases. Interestingly, these effects appear to be less exaggerated at the thruster body, resulting in a relatively constant body floating potential. In the isolated configuration, the body is not directly exposed to the high plasma potentials of the source region. Instead, the body interactions with the plasma in the near-field plume. In the near-field, the magnetic nozzle still has a strength of 200-300 G [4], which will help confine the electrons away from the body. Furthermore, the plasma experiences a potential drop and a corresponding decrease in electron temperature. These two effects may explain why the body floating potential is lower than that of the source region wall and less sensitive to changes in upstream plasma properties.

When these two components are connected, we see that the potential assumes a value between the isolated body and wall values. This is an intuitive result, as we would expect the floating potential of the connected configuration to be a balance between each isolated floating potential. However, the connected potential is more similar to the isolated wall than the body. This suggests that the loss currents to the wall of the source dominate those to the body and correspondingly, have a larger impact on the connected current balance. As we have discussed previously, the wall of the source region and thruster body are exposed to two regions of the plasma with differing plasma potentials, electron temperatures, and plasma densities. Therefore, electrically connecting these two components and enforcing equipotential alters the plasma interaction with the thruster surfaces. Currents between the two components can then offset to maintain zero net current to the thruster. We see that the potential at the source wall decreases, causing more electrons in the source to be rejected but allowing for a larger ion current to the wall. At the same time, the body potential is increased compared to the isolated case. We expect that this increase in body potential for the connected configuration would correspond to a greater electron current collected to the external surface of the thruster. We expand on this possibility in Sec. V.

Notably, as the power increases in the connected case, the equilibrated potential of the body and walls also increases with power. This mirrors the trends in the discharge channel when the two surfaces are isolated; however, this increase is less dramatic and only ranges from potentials of 100 V to 130 V.

Figure 5(b) shows the current measured across the shunt resistor when the thruster body and source region are connected. We observe a positive current flowing between the two components. According to the circuit diagram of the connected configuration, shown in Fig. 3(b), a positive current is indicative of electron current in the direction from thruster body to the plasma source. The value of this current increases as a function of input power, and trends with floating potential of the thruster body. This current seemingly confirms the speculation that electrons are being lost to the thruster body in the near-field plume. This in turn will cause ions to reach the wall of the source region to maintain the zero current condition. We further elaborate on the physical implications of this current in Sec. V.

2. Global Performance Comparison

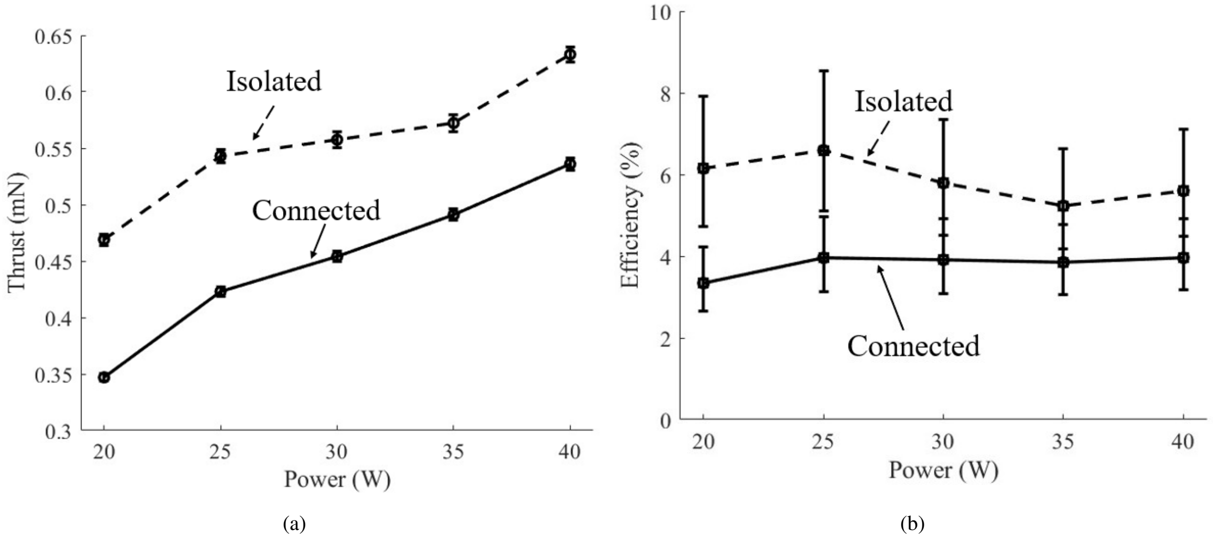

Fig. 6 (a)Thrust as a function of delivered power for the isolated and connected electrical configurations. (b)Total efficiency as a function of power for the isolated and connected configurations

In Fig. 6(a), we show thrust measurements for the two electrical configurations tested. As can be seen, the thrust increases by 25% when the source region and thruster body are electrically isolated. These results qualitatively support previous speculation that performance improves when current pathways between the thruster body and source region are eliminated [10, 11, 16]. Fig. 6(b) shows the thruster efficiency calculated from our thrust stand measurements. This metric also improves when the thruster components are isolated. The largest discrepancy is observed at the 25 W operating condition, where the measured average efficiency of the isolated test article is 50% greater than the connected. As we discuss in Sec.VII, the uncertainty in these efficiency measurements is elevated due to the accuracy of our power measurement tools. With that said, at the same commanded power operating condition, both thrust and total efficiency improve when the thruster components are isolated. In the following sections we examine the plasma properties of the device in an attempt to better understand the effects of isolating the source region.

3. Far-Field Plasma Properties

In this subsection, we compare several of the plasma properties measured by our far-field probes. The first property examined is the far-field ion energy, measured by our RPA. In Fig. 7(a), we plot the mean ion energy as a function of thruster power for both the isolated and connected tests. In this plot, the mean ion energy has been corrected for plasma potential based on Langmuir probe measurements [18].

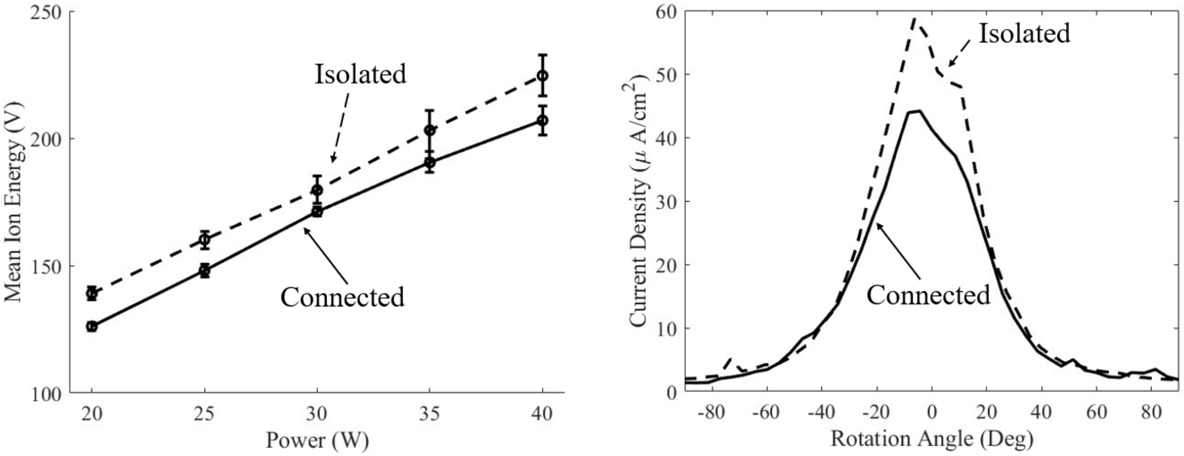

(a)

(b)

Fig. 7 (a)Comparison of most probable ion energy as a function of power. (b) Example Faraday probe traces, each taken at 30 W operating power

We first comment on the trend in average ion energy as a function of power. In both tested configurations, the ion energy increases with thruster power. We do observe a small difference in average ion energy between the two configurations. Generally, the ion energy in the connected configuration is approximately 5% lower than isolated. However, when considering the uncertainty of the plasma potential measurements and variability between RPA traces, the difference in ion energies between the two cases is minor. These results indicate that the accelerating potential, at least along centerline where these measurements are taken, is largely unaffected by the electrical configuration of the thruster. Because the acceleration mechanism of the magnetic nozzle relies on conversion of electron thermal energy, the similarities in ion energies may support the idea that centerline electron temperature is fixed for a given input power. Indeed, this discrepancy is ultimately insufficient to explain the difference in thrust (25%) between the two electrical configurations. We return to the discussion of these ion energy measurements and their similarity in Sec. V.

Having ruled out major differences in ion energy, we next examine the data from one of our other plasma diagnostics, the Faraday probe. Two sample Faraday probe traces are shown in Fig. 7(b). These traces were each taken at flow rates of 1 SCCM-Xe and delivered powers of 30 W. We note here that while the probe traces did vary as a function of power, the trends we highlight here were consistent at all powers tested. We thus only show this representative case for comparison. With this in mind, we first comment that the traces share similar shapes, with a slight asymmetry near thruster centerline. This feature has been observed in previous experiments with this thruster and similar test articles studied elsewhere [10–12]. Despite their similar shape, however, we see the isolated configuration results in a peak current density that is nearly 1.5 times higher than the connected configuration. Moreover, throughout the angular range of −35° to 35° the current density with the isolated configuration increases compared to the electrically connected state.

This result may qualitatively suggest that wall loss currents cause decreased plasma density and lower ion currents in the thruster. This difference in ion current is also consistent with our global performance measurements, indicating that the increased ion current is the primary physical mechanism by which thrust increases for the isolated configuration. To further expand on this possibility, in the next subsection, we use these probe measurements to complete our efficiency mode analysis for all operating powers tested.

4. Efficiency Mode Analysis

In Fig. 8, we plot each efficiency mode as a function of input power. For comparison, the connected configuration is plotted as solid lines and the isolated efficiencies are dashed.

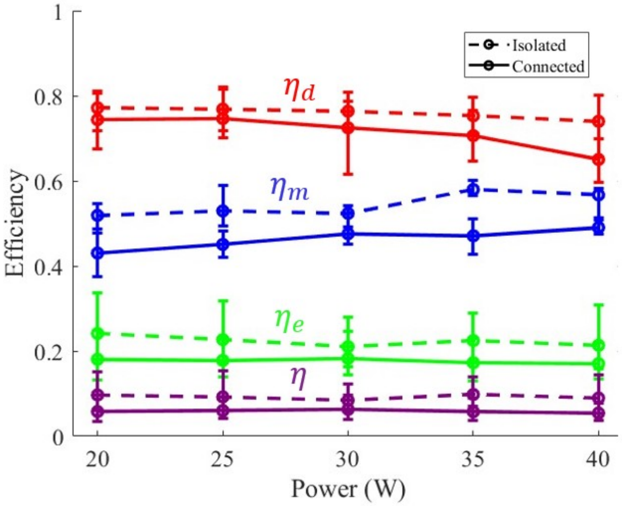

Fig. 8 Efficiency modes as a function of delivered power. Efficiencies of the connected configuration are plotted as solid lines, isolated efficiencies are dashed.

We begin by recognizing results common to both tested configurations. We see that for both cases, the ordering of the efficiency modes is the same. Divergence efficiency is the largest, followed by mass utilization and energy efficiency. Across the limited power range tested here, we find that the efficiency modes do not display strong scaling with power. Minor trends can be observed, such as a slight decrease in average divergence efficiency and an increase in mass utilization. However, when considering the uncertainty in our measurements, the significance of these trends is weakened.

Comparing efficiency modes between the cases, we first see that divergence efficiency is similar between the two cases. This is particularly true at powers below 35 W. At 35 W and 40 W, the average divergence efficiency of the connected case is 8% lower than the isolated case. Although this observation may suggest that the connected configuration results in a more divergent plume at higher powers, the difference between these divergence measurements is not beyond uncertainty.

The next efficiency mode, mass utilization, does display a difference between configurations. Consistent with our previous discussion of the sample Faraday probe traces, we find that mass utilization efficiency is as much as 20% greater for the isolated configuration than the connected. This supports the suggestion that isolating the thruster body and source wall leads to increased ion current (and thus charge carriers contributing to thrust) in the far-field plume.

Turning our attention to energy efficiency, we note that the average energy efficiency also is increased for the isolated test article. Examining Eq. 4 in the context of our previous discussion of far-field plasma properties, we can better understand this result. We see that for a given input power, energy efficiency is a function of the most probable ion energy and total ion current. We previously found that the ion energies between the two cases were similar, while the ion current is higher for the isolated configuration. The increased ion current in turn increases the average value of the energy efficiency for the isolated thruster. However, we also note that the difference in average energy efficiency values is on the order of 5%. Unfortunately, given the number of experimental measurements that are included in the energy efficiency calculation, we are unable to resolve this increase beyond uncertainty.

Finally, examining the total efficiency determined from our far-field diagnostics, we find that average total efficiency increases when the thruster body and wall are isolated. In this way, we recover the trends seen in our global performance measurements. As with energy efficiency, error propagation causes large uncertainty on the probe-derived efficiency calculations. We note here that the total efficiencies determined from our probes are, on average, higher than the efficiencies from our global performance metrics. The probe efficiency values are typically 2%-3% higher than the direct thrust measurements. This disagreement between far-field probe and global efficiencies has been well documented for ECR thrusters and represent an active area of research in the characterization of these devices[8, 11, 21]. The current hypothesis is that the large negative bias voltage (>-300 V) required to maintain ion saturation causes increased, erroneous, ion current in the wings of the Faraday probe sweep. The result is an over prediction of ion current along with over estimation of mass utilization and energy efficiency [21]. Although we have attempted to correct for this potentially erroneous current using the subtraction methods described in Sec.VII, it is possible that this effect requires additional consideration beyond our current treatment. With that said, accounting for the uncertainty of the probe and direct thrust measurements, we find these efficiencies tend to agree within error. Furthermore, the performance trends in our far-field probe measurements match those of our thrust stand measurements. We therefore conclude that the far-field diagnostics are indeed capturing the relevant changes in plasma properties that cause the measured changes in global performance such as thrust and total efficiency.

In this section, we presented results from our experimental characterization of two different thruster electrical configurations. Our global performance measurements suggest that thrust increases by 25% when the thruster body is isolated from the walls of the plasma discharge chamber, corresponding to a 50% increase in total efficiency. Far-field probe measurements show comparable ion energies between the two electrical configurations. However, ion current in the plume is increased for the isolated configuration. Consistent with this observation, our efficiency mode analysis points to increased mass utilization and, to a lesser extent, elevated energy efficiency as the drivers for improved performance of the isolated test article.

Physically, these results indicate that the isolated configuration increases the number of thrust-producing ions present in the plume. Our measurements of a 35-55 mA current between the thruster body and source region wall support this notion of significant plasma losses to the walls in the connected configuration. Isolating these two components eliminates the current pathways between components, necessary to maintain zero net current to the thruster. This effectively reduces the plasma species lost to the walls. However, even in the isolated configuration, each independent component can have non-local loss currents. To further investigate this effect, in the next experiment, we attempt to completely eliminate plasma loss currents to the thruster body with the addition of a dielectric plate in the exit plane.

B. Addition of a Downstream Dielectric Plate

The results of the previous section confirm the presence of an electron current from the thruster body to the source region. The data also suggests that performance improves when this current pathway is eliminated by isolating the components. In this section, we again compare the isolated and connected electrical configurations. However, in this set of experiments, we add a dielectric plate to the exit plane of the thruster. The intention here is to provide another mechanism for eliminating the current path from body to wall.

1. Floating Potential Comparison and Wall Current Measurements

We plot in Fig. 9(a), the floating potentials of the thruster in both electrical configurations with the addition of a dielectric plate. We immediately note that there is virtually no difference between the floating potential of the connected thruster and potential of the isolated source wall. This is contrary to the results of the previous test, where connecting the components reduced the potential compared to the isolated case. The similarity between the two electrical configurations suggests that the plate is eliminating most of the electron current from the plasma plume to the thruster body. In the previous test, we suggested that connecting the two components altered the floating potential due to non-local currents between the source wall and thruster body. However, if the thruster body does not collect any current, the floating potential will remain relatively unchanged, regardless of electrical configuration. We return to this discussion in Sec. V.

We also observe that the floating potential of the thruster body exhibits a negative value when isolated with the dielectric plate. These negative floating potentials indicate that the local plasma potential near the body is low. This also supports the conclusion that the coupling between the thruster discharge and the body is largely eliminated, since the body is insulated from the high potential plasma present in the thruster plume.

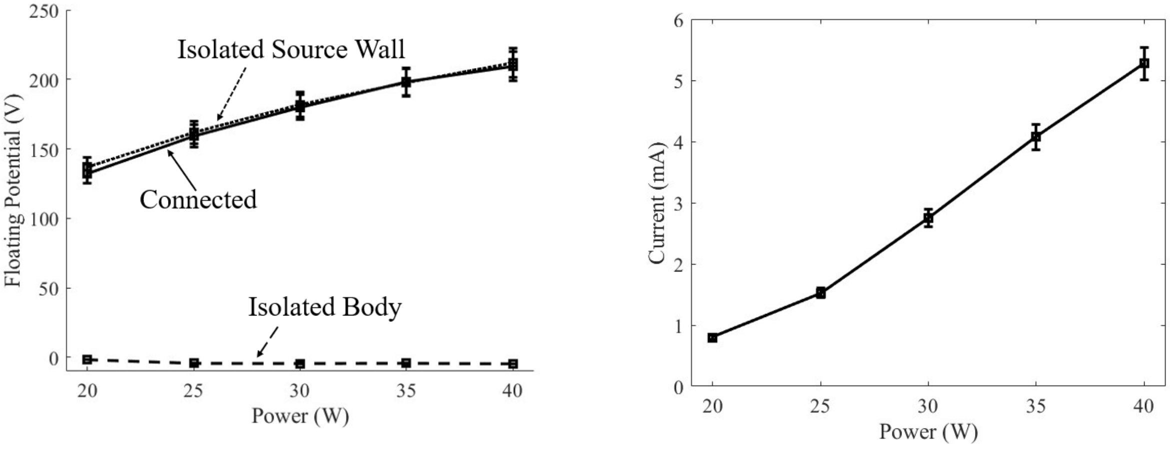

(a)

(b)

Fig. 9 (a)Comparison of floating potentials of thruster components with a dielectric plate at the exit plane. (b) Measured current between the thruster body and source as a function of delivered power with a dielectric plate.

To this point, we see when examining the current measurements in Fig. 9(b) that the magnitude of currents through the thruster body is an order of magnitude lower than when the dielectric plate is not in place.

2. Global Performance Comparison

We next compare, in Figure 10(a), the thrust produced for each electrical configuration when the dielectric plate is added to the thruster exit.

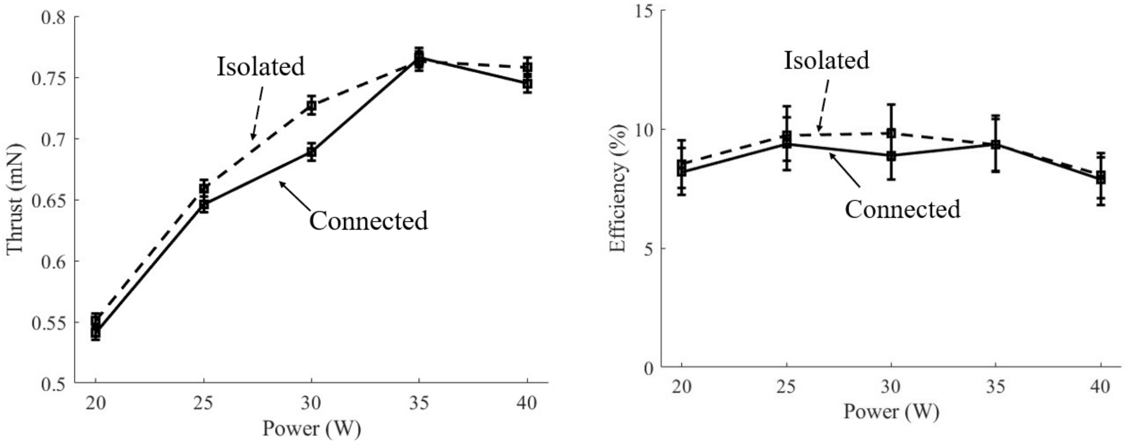

(a)

(b)

Fig. 10 (a)Thrust as a function of delivered power for both electrical configurations with a downstream dielectric plate. (b)Total efficiency as a function of power with a downstream dielectric plate.

Unlike the previous experiment, when the dielectric plate is added, we find that performance no longer depends on electrical arrangement of the internal thruster components. At nearly every power tested, the thrust measurements of the isolated and connected configuration agree within uncertainty. A similar result is found when examining the total efficiency measurements in Fig. 10(b). We thus conclude that addition of the plate has eliminated the physical mechanism responsible for the performance difference observed in Sec. IV.A.2.

When comparing these global performance measurements to the previous experiment, we find that thrust is increased by a factor of 1.5 above the connected configuration and 1.2 above the isolated test. Total efficiency with the plate increases to almost 10% at 30 W with the plate, compared to 4% and 5.75% in the connected and isolated configurations respectively. This improvement, even over the isolated configuration, supports the hypothesis that there are additional loss mechanisms occurring at the isolated, conductive body. We return to this point in Sec. V. We note, however, that this increase in performance when the dielectric plate is added agrees with previous experimental results taken on other test articles [11].

3. Far-Field Plasma Properties

As we did with the electrical configuration test, we examine the data from our far-field plasma diagnostics. However, in this case, given the similarity in global performance between the connected and disconnected configurations, we expect the far-field plasma properties to be very similar.

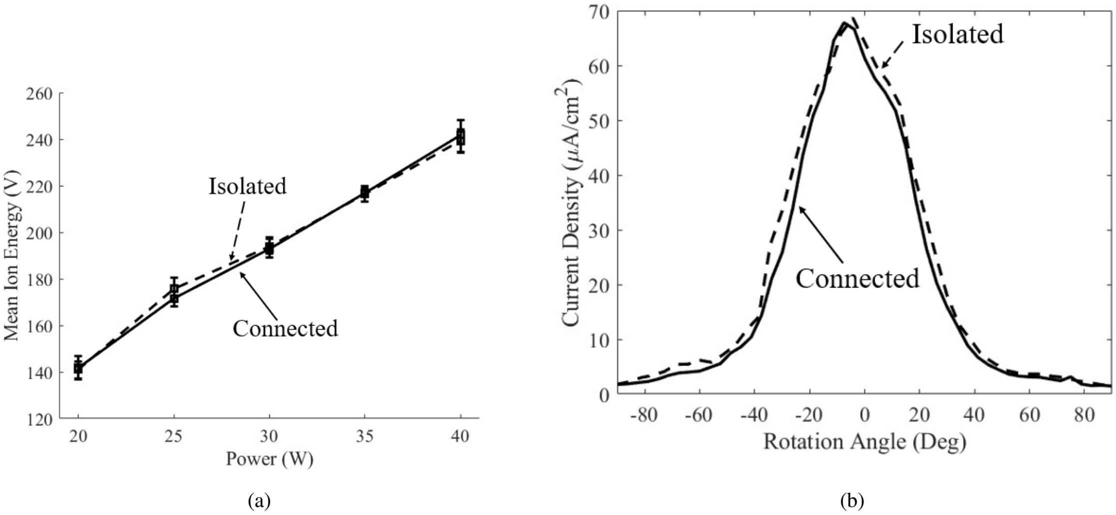

(a)

(b)

Fig. 11 (a) Ion energy measurements as a function of power for the connected and disconnected configurations with a dielectric plate downstream. (b) Comparison of Faraday probe sweeps for each electrical configuration with the dielectric plate downstream. Both traces are taken at 30 W.

To this end, examining Fig. 11(a), we find that the most probable ion energies measured by our far-field RPA are nearly identical. In a similar way, the ion current profiles between the two cases are also very similar. Qualitatively, these plots exhibit similar trends to the previous measurements. Mean ion energy increases as a function of power and the Faraday probe traces are similar in shape, including the centerline asymmetry. However, there are quantitative differences between this data and the previous section. Comparing the values of these ion energies to the previous experiment, we find that the most probable ion energies are increased by approximately 10% compared to the isolated case and 14% compared to the connected configuration of the previous test. Additionally, the peak ion current density is 16% greater than the isolated test and 45% larger than the connected configuration. Each of these findings agree with the elevated global performance measurements obtained from the thrust stand.

4. Efficiency Mode Analysis

To conclude, we present the efficiency mode analysis with a dielectric plate attached to the thruster body. Figure 9 shows the efficiency modes as a function of power for each configuration tested. Solid lines represent the connected configuration with the dielectric plate, while dashed lines show the isolated configuration with the plate. As expected from our global performance measurements, the efficiency modes of each configuration match very closely at all powers tested. Although the isolated configuration with the plate does show minor improvement over the connected efficiencies, the differences in these measurements is well within measurement uncertainty.

As was the case for the previous experiment, the efficiency modes are ordered with divergence efficiency being the

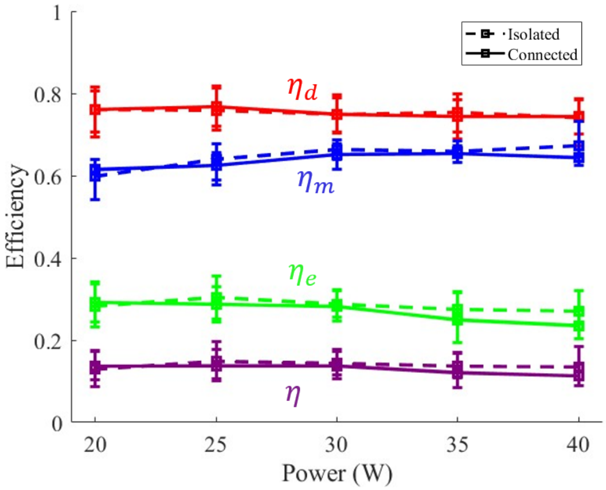

Fig. 12 Efficiency modes as a function of power with the downstream dielectric plate. Efficiencies of the connected configuration are plotted as solid lines, isolated efficiencies are dashed.

highest, followed by mass utilization and energy efficiency. From these results we can more clearly see trends in the efficiency modes as a function of power. Once again divergence efficiency remains approximately constant, with a very slight decrease of less than 2% across the power range tested. However, mass utilization does monotonically increase as a function of power, rising 10% across the 20 W range tested. The opposite trend is observed for energy efficiency, which decreases with power, and is lowered by 5% over the power range. The opposing trends between mass utilization and energy efficiency suggest that performance will not monotonically increase with power. Indeed, there is a balance between increasing plasma density, and losing plasma to the walls. At higher powers, we may not appreciably increase our plasma density, but we may lose more species to the walls, decreasing performance. These trends in efficiency modes have been observed in this test article before, and more closely match the behavior seen when testing with the anodized thruster body [8, 10, 11].

To provide a better comparison, we plot in Fig. 13 a bar chart of efficiency modes for all four thruster configurations tested. We perform this comparison at the nominal operating condition of 30 W delivered power at 1 SCCM-Xe.

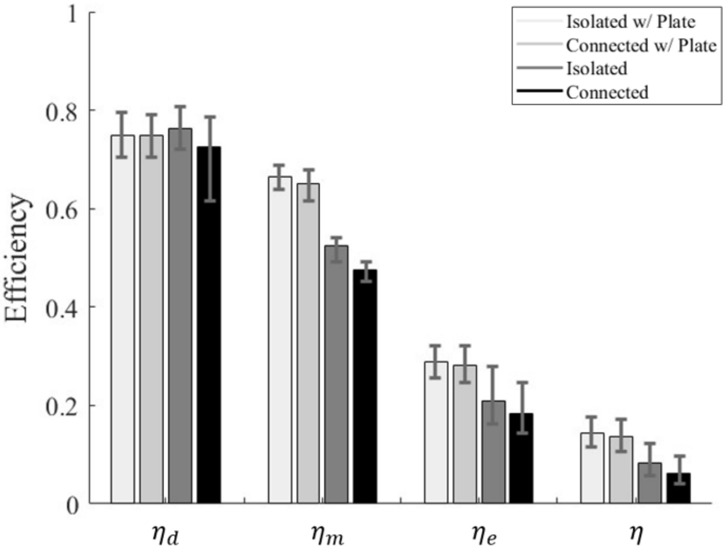

Fig. 13 Comparison of efficiency modes between all thruster configurations tested at 30 W, 1 SCCM-Xe

We first comment that divergence efficiency with and without the plate remains comparable at about 75%. This is unsurprising given that we expect plume divergence largely to be a function of the topology of the magnetic nozzle, which is unchanged between the four configurations studied here. Consistent with our comparison of far-field plasma properties, both mass utilization and energy efficiencies are increased with the addition of the dielectric plate. Because these two efficiency modes are higher, total efficiency is also higher when the dielectric plate is present. This too is consistent with our previous data, where we observed thrust was increased for the dielectric plate compared to either of the previously tested configurations. As was the case in our previous efficiency mode analysis, we find that the probe data yields efficiency values 2%-3% larger than our thrust measurements. However, we again find that our global performance trends are recovered in our probe data.

In this section, we showed the results of our experiments using a dielectric plate to minimize the current collection area of the thruster body. With the addition of the dielectric plate, no dependence on internal electrical configuration is observed. Furthermore, when the thruster body and source region are connected, we find that the plate reduces the current between these two components by an order of magnitude. Compared to both electrical configurations tested in our previous experiment, we find that the dielectric plate improves performance. These improvements are reflected as an increase in both far-field ion energy and ion current with the dielectric plate in place. In our efficiency mode analysis, tests with the dielectric plate yield higher mass utilization and energy efficiencies, resulting in higher total efficiencies.

Consistent with the results of the previous experiment, the main conclusion drawn from tests with the plate is that performance improves when loss current pathways are eliminated. Interestingly, we find that the addition of the plate improves performance, even compared to the isolated electrical configuration. This is despite the fact that both the body isolation and the plate eliminate losses between the thruster body and source walls. Physically, this suggests that there are additional loss mechanisms taking place at the thruster body, even when the body is isolated from the source. Indeed, in this case, the body is manufactured of a conductive material, allowing for loss currents to form within the thruster body itself. Addition of the dielectric plate isolates the body from the plasma plume, eliminating this body loss current. In the next section, we continue our discussion of loss currents in the thruster. We use thin sheath theory to perform a quantitative analysis of these currents and compare them to our experimental findings.

V. Discussion

The data presented in the previous section highlights differences in performance depending on the electrical arrangement of the thruster. In each test, elimination of current pathways improved performance. In the electrical configuration test, this was accomplished by isolating the thruster body from the source region wall. In the second test, this was done by adding a dielectric plate to the thruster exit plane, effectively isolating the surface of the thruster body from the plasma. In this section we provide further physical insight as to why these changes affect thruster performance. We revisit each experiment and explore the physical reasons for our experimental observations.

A. Effects of Thruster Electrical Configuration

Consistent with our hypothesis presented in the introduction of this work, we find that performance improves when the source region wall is isolated from the thruster body. Along with an increase in thrust, we observe differences in floating potential of thruster components when the electrical configuration is changed. This change to potential structure, alters the sheath dynamics in the source region and near field plume of the thruster, resulting in the observed behavior. We explore these sheath dynamics in the ensuing discussion.

1. Isolated Configuration Sheath Dynamics

As discussed in Sec. II, the surfaces of the thruster must maintain a zero net current condition. In other words, the ion current to the surfaces, I_i must be equal and opposite the electron currents, I_e. The primary purpose of the plasma sheath is to maintain this zero net current condition. These currents can be described using thin sheath theory [18],

$$I_e = qn_eA\sqrt{\frac{qT_e}{2\pi m_e}}\exp\left(\frac{V_f - V_p}{T_e}\right), \tag{6}$$

$$I_i = qn_eA\sqrt{\frac{qTe}{m_i}}. \tag{7}$$

In these equations, q represents the fundamental charge, n_e is the plasma density, A is the collection area of the boundary that forms the sheath, T_e is the electron temperature, V_f is the floating potential of the surface, V_p is the local plasma potential, and m_i and m_e are the ion and electron mass respectively. For a single component, the zero net current condition enforces $I_e = I_i$. We use this current balance to evaluate the losses to the walls for each electrical configuration tested.

We first examine the current to the wall of the source region in the isolated configuration. This current balance will largely be dictated by Eqns. 6 and 7. However, the electron behavior is complicated by the strong magnetic field, which confines electrons away from the walls. The physics that dictate diffusion across these field lines is complex and an ongoing area of research[11, 22]. As a simple method to account for this, we introduce a confinement factor, $0 < c < 1$, which limits the electron current to the wall according to $I_e = (c)qn_eA\sqrt{\frac{qT_e}{2\pi m_e}}\exp\left(\frac{V_f - V_p}{T_e}\right)$ [14]. This approach has previously been used in models of the ECR source region to describe the density profile in the presence of the strong magnetic field [23]. We can then equate this moderated electron current with 7. The resulting expression reduces to

$$\frac{V_f - V_p}{T_e} = \ln\left(c\sqrt{\frac{m_i}{2\pi m_e}}\right). \tag{8}$$

From our experimental data, we have direct measurements of the floating potential at the wall. Additionally, we can approximate the plasma potential in the source region using our far-field RPA data. We assume that the plasma potential in the source is equivalent to the total retarding potential observed on the probe. This value differs from the ion energy, since we are not correcting here for far-field plasma potential. Treating c as a free parameter, we are able to solve for electron temperature. Unfortunately, the electron temperature inside the plasma source region of the ECR thruster has yet to be experimentally characterized. Therefore, we tune the c coefficient based on electron temperature estimates from global discharge models and far-field measurements [24, 25]. Good agreement is found for $c = 0.03$, which yields electron temperatures ranging from 20-50 eV over the power range tested.

Similar to the walls of the plasma source, the isolated thruster body will establish a floating potential that preserves zero net current. However, the plasma properties in the vicinity of the thruster body will be different than those in the thruster source region. As a result, we must next solve for electron temperature near the thruster body. To do so, we use a formulation similar to Eq. 8. However, we no longer implement the confinement factor, c. Although the magnetic nozzle does confine the plasma in the near field, the strength of the field near thruster exit is approximately three times weaker than in the source. Therefore, we use the unmodified expression for electron current shown in Eq. 6. Solving this equation for electron temperature at the thruster body requires knowledge of the local plasma potential. In our experimental setup we did not directly measure plasma potential in the near-field. Instead we rely on previous LIF measurements, which have characterized the potential structure near the thruster exit[26]. These measurements found that the plasma potential decreased to less than 60% of the potential in the source region within 2.5 cm of the thruster exit plane. We therefore assume $V_{p_{body}} = 0.6V_{p_{source}}$ for our calculation of electron temperature adjacent to the thruster body.

Finally, to determine the scaling of these loss currents as a function of power, we must have knowledge of the densities. Here we assume a density ratio between the plasma collected by the thruster source and body. We parametrically vary this density ratio to determine the effects on the current balance. Subject to these assumptions, we solve for the currents to both the source region wall and the thruster body as a function of input power. We plot the results of this analysis in Fig. 14(a).

We first comment on the trend in these loss current as a function of power. Both current lost to the isolated wall and isolated body increase as a function of power. This increase in loss current is primarily an effect of increased electron temperatures at higher input powers. These elevated temperatures drive higher plasma potentials and also increase the potential drop across the plasma sheath. The result is an increase in current to the wall. Generally, the electron temperatures determined by solving Eq. 8 show a direct increase in electron temperature as a function of power. Between 20-25 W our results do show a few eV decrease, resulting in the slight current drop seen in Fig. 14(a). Above 25 W we find that the temperature of the plasma in the source increases more rapidly with power than the temperature near the body. As a result, at high powers, current lost to the source region wall dominates. Our next observation relates to the relative values of the currents to the body and the wall. We plot the ratio of body current to wall current for various density ratios in Fig. 14(b). We find that, for density ratios less than 0.4, the current to the radial wall of the source region is greater than the losses to the body. This result is intuitive given that the walls of the source region are directly in contact with the highest density and highest temperature region of the plasma discharge. However, as we increase the assumed density near the body, we find that losses to the body dominate. This effect is partially due to the increased collection area of the body, which is 2.5 times greater than the source wall. Even when assuming that the density at the body is an order of magnitude lower than that of the source, we find that the ratio of loss to the body

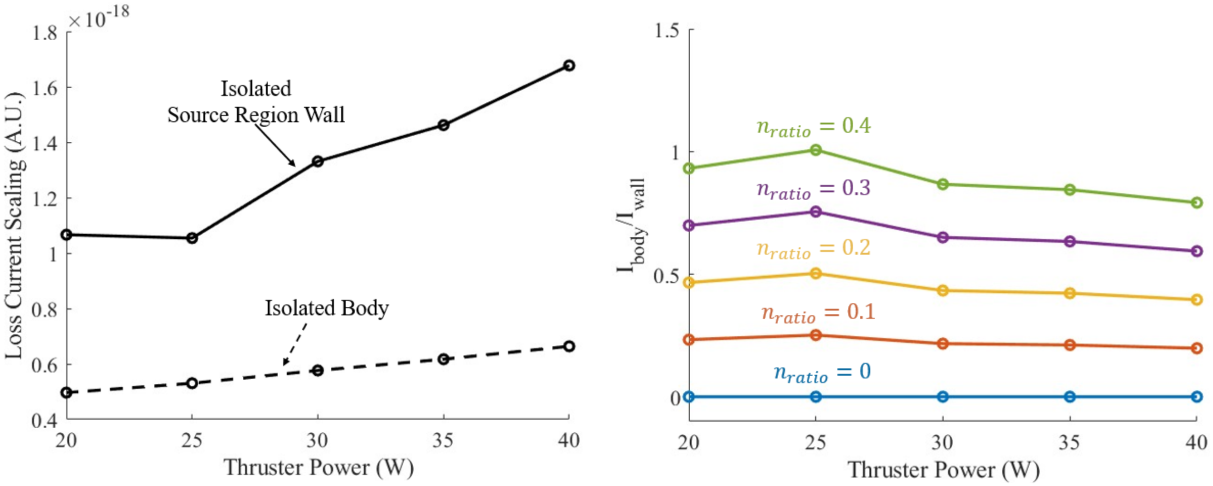

(a)

(b)

Fig. 14 (a) Scaling of current losses to isolated components as a function of power for a representative density ratio of 0.3. (b) Ratio of current lost to the body over current lost to the wall for multiple density ratios between the collection points of the source region and thruster body.

compared to the source is greater than 20%. This supports the hypothesis that there are additional losses taking place to the isolated thruster body and we return to this point in our discussion of the dielectric plate tests.

2. *Connected Configuration Sheath Dynamics*

When the two thruster components are electrically connected, we must modify our description of the zero net current condition. In this case, the total ion and electron current collected by all thruster components must be balanced. This total current balance will take the form,

$$I_{e_w} + I_{e_b} = I_{i_w} + I_{i_b} \tag{9}$$

$$(c)n_{e_w} A_w \sqrt{\frac{qT_{e_w}}{2\pi m_e}} \exp\left(\frac{V_{f_w} - V_{p_w}}{T_{e_w}}\right) + n_{e_b} A_b \sqrt{\frac{qT_{e_b}}{2\pi m_b}} \exp\left(\frac{V_{f_b} - V_{p_b}}{T_{e_b}}\right) = n_{e_w} A_w \sqrt{\frac{qT_{e_w}}{m_i}} + n_{e_b} A_b \sqrt{\frac{qT_{e_b}}{m_i}}. \tag{10}$$

Here we have modified Eq. 6 and 7 with subscripts $_w$ and $_b$ to reflect the differing plasma properties between the source region wall and thruster body, as well as the differing collection areas. Connecting these components enforces the same floating potential at both surfaces. As we found in Fig. 5, the resulting potential falls in between the floating potential of the two components. A more positive potential is enforced on the thruster body, while the source wall becomes more negative.

To determine the effects of connecting these components, we again turn to the scaling of loss currents. Unlike the previous current balance, we are unable to directly solve for electron temperatures in the relevant region. We instead assume that the electron temperature in the source remains constant between the isolated and connected configurations. This assumption is supported by our measurement of similar ion energies in the far-field, as well as the expectation that electron temperature in the source is largely a function of thruster operating power. As before, we use the far-field RPA measurements to inform the plasma potential in the source region and rely on the LIF data of Ref. [26] to assume $V_{p_b} = 0.8V_{p_s}$. Subject to these assumptions, we can solve for T_{e_b} and determine the resulting loss currents.

In our isolated configuration testing, we compared the calculated current losses for the body and source. In that case, since each component was floating, the ion and electron currents balanced for both. In the connected configuration, that is not the case, different components of the thruster can preferentially collect different species. To illustrate this point, we plot the scaling of the ion and electron currents in 15(a) and (b) respectively.

From these plots we find that we recover several of the trends found in our experimental results. Firstly, we indeed find that the losses to the body are dominated by electron current, while the source wall primarily collects ions. This is consistent with the observed change in floating potential between the isolated and connected cases. The potential on the thruster body becomes more positive, leading to increased electron current. Conversely, the potential of the source region wall becomes more negative, rejecting more electrons, but allowing for increased current losses to offset the large increase in electron current to the body. We also note that the loss currents generally increase as a function of power. This is consistent with the experimental loss current measurements presented in Sec. IV.

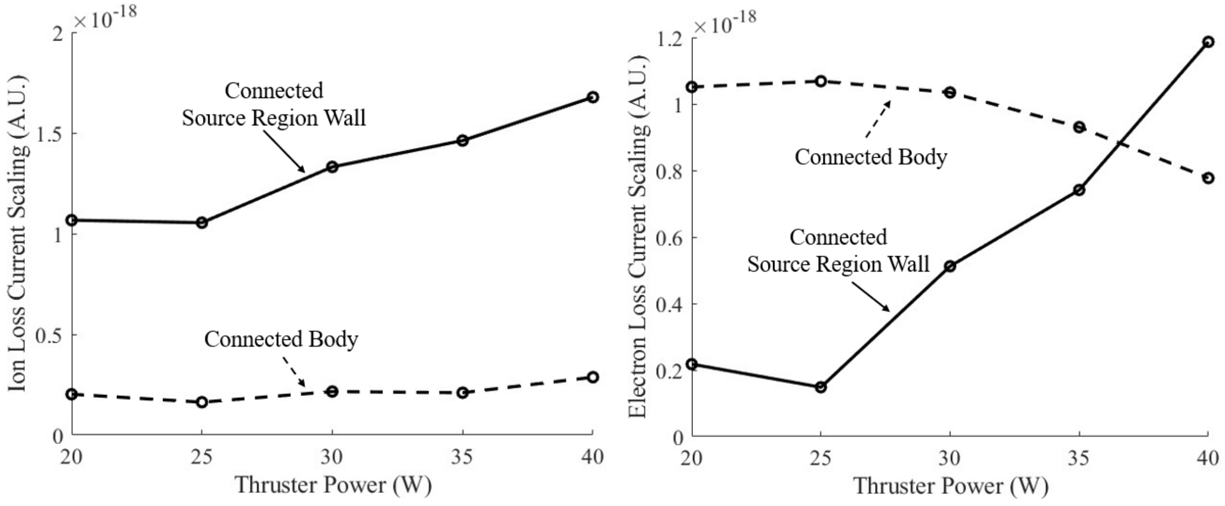

(a)

(b)

Fig. 15 (a) Scaling of ion current losses to isolated components as a function of power for a representative density ratio of 0.3.(b) Scaling of electron current losses to isolated components as a function of power for a representative density ratio of 0.3.

Although these theoretical results qualitatively match our expectations, several strong assumptions are employed, which make it difficult to confidently compare magnitudes of total loss currents to our experiment. This also complicates a comparison between the isolated and connected configurations. In this approach we have enforced a constant electron temperature in the source between the isolated and connected tests, as well as a fixed potential ratio between the source and body. In reality, changing the electrical configuration of the thruster may alter these plasma properties. A more confident determination of loss currents will require measurement of near-field plume properties, including plasma density and electron temperature. These measurements would be highly informative for further characterizing loss mechanisms near the source region of the thruster.

B. Estimation of Power Loss from Experimental Measurements

Although we are unable to confidently determine the magnitudes of the relevant current losses from our thin sheath theory, by directly measuring the current between the thruster body and source region, it is possible to estimate the power loss associated with these wall currents. Our data suggests that electron current is flowing from the thruster body to the source region. To balance this effect, and maintain a zero net current condition to the wall, an equal ion current must stream from the plasma to the walls of the plasma chamber. Therefore, following the electrical convention of current opposing the direction of electron flow, "electrical current" travels from thruster source to body.

The power carried by this current can be estimated using circuit analysis as $P_{loss} = I_{loss}\Delta V$, where ΔV is the potential drop the ions experience as they reach the wall. This potential drop can be estimated based on our experimental data. From thruster floating potential measurements, we know the voltage at the wall of the plasma source region. We then argue that the plasma potential will be equivalent to the retarding voltage observed by our RPA probe. Because our floating potential is ground referenced, we use the absolute retarding potential observed in our RPA trace. Crucially, this is different than the mean ion energy, since the ion energy analysis accounts for residual plasma potential measured by our Langmuir probe. The potential drop experienced by the ions is then taken as the difference between the source plasma potential and the floating potential at the walls. Performing this calculation, we are able to plot the fraction of input microwave power that is lost in driving these wall currents. We show these results in Fig. 16, with error bars

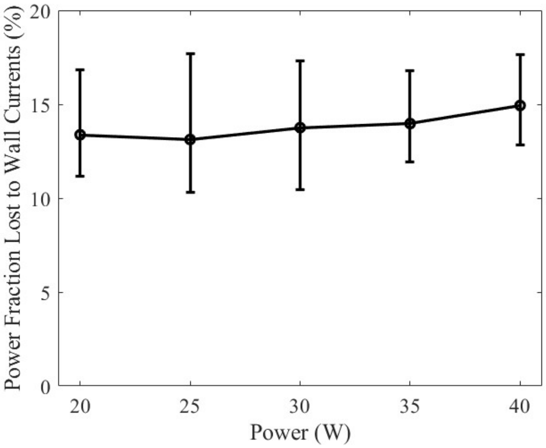

Fig. 16 Estimated power loss due to wall currents as a fraction of the input microwave power.

representing uncertainty in thruster power and far-field probe measurements. This analysis shows that when the source region and thruster body are connected, over 10% of the input power is lost to maintain zero net current on the thruster. This power loss to the walls can be seen in our efficiency breakdown as a decrease in energy efficiency. In particular, power lost to the walls does not serve to accelerate ions, therefore, the metric of input microwave power to ion kinetic power is reduced in the presence of these large wall currents. Furthermore, this current also corresponds to a reduction in plasma density as current arises from species lost to the walls. This is reflected in our far-field probe data as a reduction in ion current, and a corresponding decrease in mass utilization efficiency when the body and plasma chamber are electrically connected. Quantification of this power loss is yet another indication of performance improvements resulting from component isolation in the thruster.

C. Effects of Adding a Dielectric Plate to the Exit Plane

Addition of the dielectric plate to the thruster exit plane results in two key findings. First, performance of the thruster improves and no longer depends on the internal electrical properties. Second, the current measured between the thruster body and source region is reduced by an order of magnitude. We discuss each of these effects in detail.

As shown in Fig. 17, the motivation for adding a dielectric plate to the thruster exit plane is to eliminate the current pathway between the near-field plume and the thruster body.

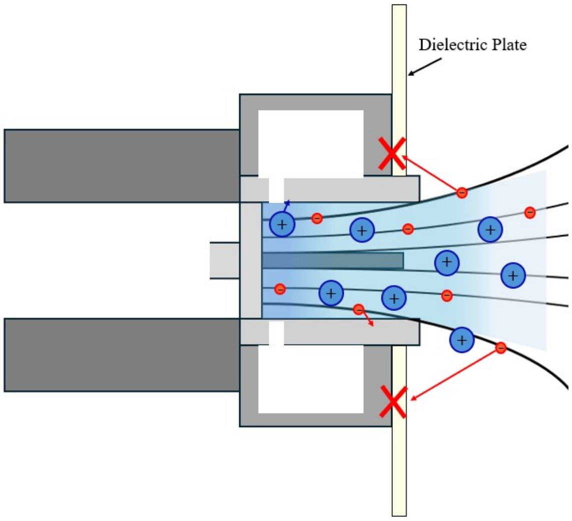

Fig. 17 Notional diagram of the downstream dielectric plate blocking loss currents to the thruster body

By placing an insulator between the plasma and the thruster body, we have caused the collection area of the body to go to zero. Examining the global current balance between connected components described by Fig. 10, we see that in the limit where $A_b \rightarrow 0$, the current balance for the connected configuration reduces to that of only the isolated wall. This theoretical elimination of collection area is consistent with our experimental results, where performance with the plate is constant, regardless of internal electrical configuration. In both cases, the only current collecting surface is the source wall.

The next observed effect, an improvement in performance, can also be understood in the context of this current balance. As we found in Fig. 14, there may be an appreciable current loss occurring at the body, even in the isolated configuration. As such, preventing the body from collecting plasma current eliminates losses from the system. To illustrate this point, we perform a similar current balance as the isolated electrical configurations. We assume the same value for c and again take the absolute retarding potential from our RPA measurements with the plate as the plasma potential in the source. We then solve for electron temperature for the operating conditions with the plate and calculate the current lost to the walls of the plasma source. We show the results of this calculation in Fig. 18 (a).

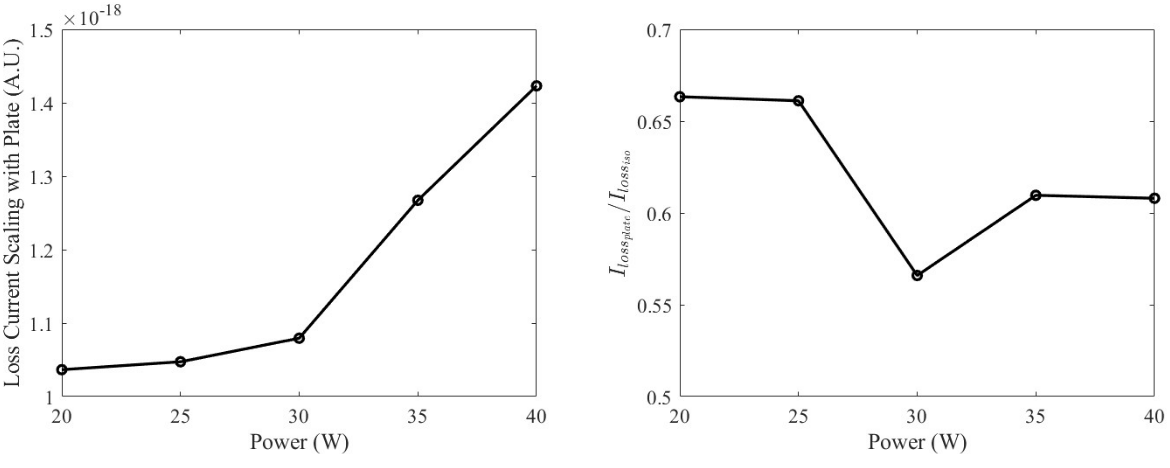

(a)

(b)

Fig. 18 (a) Current loss scaling to the source region walls as a function of power with the dielectric plate. (b) Total wall loss current with the dielectric plate represented as a fraction of total loss current in the isolated configuration. A representative density ratio of 0.3 is used for the isolated analysis

Similar to the loss currents in the isolated electrical configuration, we find here that the current lost to the wall increases monotonically with power. As before, this is primarily a result of the increased electron temperatures at higher input powers, which we find by solving Eq. 8. In Fig. 18(b), we compare the total loss currents between the plate and isolated configurations. For this comparison, we have determined the total loss current in the isolated configuration to be the sum of the losses to the isolated wall and body, $I_{loss_{iso}} = I_{wall_{iso}} + I_{body_{iso}}$. We find here that, subject to the same assumptions about our sheath dynamics, addition of the downstream plate reduces the total current lost. Although the exact value of this reduction will depend on the density ratio between thruster body and source, minimizing the collection area of the body ultimately reduces total current losses. Furthermore, because current to the body also increases monotonically with power, we find that elimination of the body collection area also reduces the fraction of total current lost at higher powers. The theoretical reduction in loss current is consistent with our experimental measurements. As presented in Sec. IV, we find that the addition of the plate reduces current between the body and wall by an order of magnitude. We also find increased performance when the plate is added. Minimizing current lost to the walls will result in increased plasma density, as well as more power deposited into the plasma. Indeed, indications of these trends can also be found in our experimental data in the form of increased ion currents and ion energies in the far-field probe measurements for configurations with the dielectric plate.

D. Comparison to Other Thruster Configurations

In our previous works, we have investigated several configurations of the UM ECR v.2 thruster. These variations have primarily considered changes to the material of the plasma source wall. To provide additional context to the performance improvements observed in this work, in Fig. 19 we compare these thrust measurements to the results of our previous wall material study [10]. An important point is that the prior measurements were taken with the anodized thruster body. All thrust measurements are taken at a flow rate of 1 SCCM-Xe.

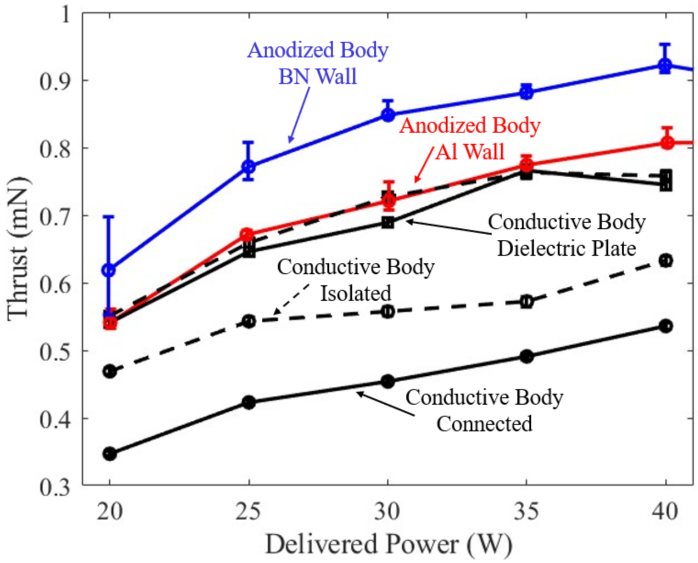

Fig. 19 Comparison of thrust measurements between the configurations studied in this work and the wall material investigation of Ref. [10]

The ordering of performance is as follows. The conductive body in the connected configuration is the lowest performing thruster arrangement tested. A performance improvement is seen when the aluminum wall is isolated from the conductive body. However, this performance remains lower than the aluminum wall with the anodized thruster body. Similar to our testing with the plate, we suspect that this difference between anodized and untreated body results from additional plasma losses to the conductive body, likely a result of non-local current loops forming within the body itself.

When a dielectric plate is added to the exit plane of the conductive body, we find that our performance measurements agree very well with the anodized body configuration for aluminum walls. This suggests that both the anodization and dielectric plate serve the same purpose of preventing non-local short circuits in the thruster body. This insight may explain the competing effects previously reported for tests with a dielectric plate. Peterschmitt found an 18% increase in thrust when a dielectric plate was placed in the exit plane of ONERA's ECR test article [11]. Hitchens later repeated this experiment on a different thruster and observed no improvement when the dielectric plate was added. It is possible that the thruster tested by Hitchens had already eliminated loss currents to the body through some other design decision, for example, coating the thruster body in a polyimide film. If this were the case, it could explain why the addition of the dielectric plate did not cause the performance improvement reported by Peterschmitt. Regardless of the mechanism, our thrust measurements show that eliminating current pathways from the plume back to the body increases thrust by over 20%.

Even once current to the thruster body is eliminated, performance can be further improved by using an electrically insulating wall material. Figure 19 shows that the highest performing configuration tested thus far has been the anodized thruster body, with BN walls. Similar to the observed improvement when anodizing the thruster body, we speculate that the improved performance for BN walls arises from elimination of non-local currents within the wall of the plasma source itself. Unfortunately, in this work we did not have the ability to measure these currents within a single component. However, we do recognize that for all thruster components, eliminating both internal and external conductive pathways corresponds to improved performance.

VI. Conclusion

ECR magnetic nozzle thrusters are one of the most promising candidates for small satellite electric propulsion. The ability of these devices to operate at low powers and eliminate the complexity of a hollow cathode make them particularly attractive for systems that are limited in size, weight, and power. However, historically, the performance of ECR thrusters has suffered to a point that it has been impractical to fly these devices.

One suspected reason for the poor performance of low-power ECR thrusters arises from loss currents traveling through the walls of the device. These non-local currents were suggested to decrease plasma density in the source region and act as a pathway for power loss to the walls. Although global measurements had previously indicated that performance of the device improves when these loss current pathways were eliminated, this effect had yet to be characterized in detail. In this work, we experimentally investigated the effects of wall loss currents in a low-power ECR magnetic nozzle thruster. We employed a test article that allowed us to control the electrical connectivity between the thruster body and plasma source wall. We then tested this device in multiple configurations and characterized both global performance and thruster efficiency modes using a combination of direct thrust measurements and far-field plasma diagnostics.

Consistent with previous global measurements, we found that thrust increased by 25% when the two components of the thruster are isolated. This change to electrical configuration was accompanied by changes to the floating potentials of the device and modified sheath behavior in the source region and near-field plume of the thruster. Comparison of efficiency modes between the two electrical configurations showed an increase to mass utilization and energy efficiency in the isolated configuration. Additionally, current measurements in the connected configuration lead us to believe that as much as 15% of the input power is being lost to wall currents when the source region is connected to the thruster body.

We repeated this experimental characterization of electrical configuration, this time with the addition of a dielectric plate in the thruster exit plane. With this addition, no dependence on electrical isolation of internal components was found. Thrust and efficiency mode measurements were nearly identical across both internal electrical configurations when the dielectric plate was added. Furthermore, measurements of current flowing between the body and source show that the plate reduced this loss pathway by an order of magnitude. We also found that performance of the thruster with the plate was higher than either electrical configuration tested without the plate. This points to loss currents that may be taking place within a single thruster component in addition to the current flowing between components measured in this work.

The results of this work point to significant performance improvements when electrically conductive thruster components are replaced with insulating materials. Across this study and our previous wall material investigation, the highest performing configuration had insulating body and source wall materials. This suggests that current losses both between and within conductive thruster components drive down performance of the device.

Acknowledgments

This work was funded by the Air Force Office of Scientific Research Space Power and Propulsion Program, under grant FA9550-25-1-0025. The authors would like to thank Miron Liu, John Riley O'Toole, Dr. Tate Gill Dr. Parker Roberts, and Dr. Benjamin Wachs for their useful discussions.

VII. Appendix: Data Processing and Uncertainty Analysis

The experimental measurements presented in this work contain a degree of uncertainty. In this section we detail the sources of this uncertainty, as well as the data processing methods used.

A. Thrust Stand Measurements

For our experiments, we utilize the pendulum-type thrust stand designed by Wachs and Jorns [27]. The stand is calibrated by applying a series of predetermined masses, which are each correlated to a voltage signal output by the optical displacement sensor. Uncertainty in these thrust measurements arises primarily from manufacturing tolerances in the thrust stand components, as well as uncertainty in the calibration value. Following the analysis detailed by Ref. [27], we can describe this uncertainty mathematically as

$$\frac{\sigma_T}{T} = \left[\left(\frac{\sigma_\delta}{\delta} \right)^2 + \left(\frac{\sigma_{k_{cal}}}{k_{cal}} \right)^2 + \left(\frac{\sigma_{l_t}}{l_t} \right)^2 + \left(\frac{\sigma_{l_{cal}}}{l_{cal}} \right)^2 \right]. \tag{11}$$

In the above expression, T is thrust value measured, k_{cal} is the measured calibration constant, l_t is the distance from the thrust stand pivot to the thruster, and l_{cal} is the length of the calibration platform. All σ terms represents the uncertainty in the quantity denoted in their subscript. As designed, l_t = 0.305m and l_{cal} = 0.102m. The uncertainty on each of these lengths is assumed to be 1 mm based on manufacturing tolerances. Uncertainty in the calibration value, $\sigma_{k_{cal}}$ was empirically determined to be $\sigma_{k_{cal}} = 5.8 \times 10^{-5} \frac{mm}{mN}$. During testing, the calibration constant, k_{cal}, is retaken between each measurement point. This procedure allows us to accurately account for changes in the spring constant of the thrust stand resulting from processes such as thermal drift.

B. Global Efficiency Measurements

Calculation of total efficiency from direct thrust measurements requires additional measurements of thruster power and flow rate. Following the characterization by Wachs of the experimental setup used in this work[4], the measured efficiency can be bounded based on uncertainty in thrust, power and flow rate measurements. The maximum and minimum efficiencies are given as

$$\eta_{max} = \frac{T^2}{2\dot{m}P_{min}}\sqrt{\left(\frac{T\Delta T}{\dot{m}P_{del}}\right)^2 + \left(\frac{T^2\Delta\dot{m}}{2\dot{m}^2P_{del}}\right)^2 + \left(\frac{T^2\Delta P}{2\dot{m}P_{del}^2}\right)^2}$$

$$\eta_{min} = \frac{T^2}{2\dot{m}P_{max}}\sqrt{\left(\frac{T\Delta T}{\dot{m}P_{del}}\right)^2 + \left(\frac{T^2\Delta\dot{m}}{2\dot{m}^2P_{del}}\right)^2 + \left(\frac{T^2\Delta P_s}{2\dot{m}P_{del}^2}\right)^2}.$$

Here, T represents thrust, P_{del} is the delivered power to the thruster, and $\dot{m}$ is the mass flow rate. ΔT is the uncertainty in thrust according to the analysis described above, $\Delta\dot{m}$ is uncertainty in the mass flow controller, typically defined by the manufacturer, and ΔP_s is uncertainty in our power measurement arising from our measurement equipment. This is in contrast to P_{max} and P_{min}, which represent the maximum and minimum possible absorbed powers for a given set point. This total uncertainty in absorbed power is a function of coupling coefficient of the thruster, and includes directivity errors arising from our bidirectional coupler measurements as well as measurement error at our power meter. Uncertainty in absorbed power dominates this analysis, as we are typically only able to measure absorbed power within 10% uncertainty. This treatment for uncertainty in our absorbed power arises in our efficiency mode analysis as well. Particularly energy efficiency. We continue discussion of the probe measurements that inform our efficiency analysis below.

C. Far-Field Probe Measurements

Previous attempts to characterize ECR thrusters have faced great difficulty with far-field probing [5, 8, 11, 21]. These challenges arise from the high electron temperatures near the central antenna, which necessitate large repelling potentials to investigate far-field ion characteristics. As a first attempt to minimize uncertainty, we collect each probe trace a minimum of three times. This practice allows us to evaluate repeatability of the probe measurements and better account for uncertainty in our diagnostic equipment. Additional uncertainty arises from the processing of each probe trace, where key plasma properties such as ion energy, plasma potential, and ion current are determined. We describe our treatment of each diagnostic in the following sections.

1. Langmuir Probe

In this work, the primary purpose of the Langmuir probe is to correct our ion energy measurements. In our experimental setup the Langmuir probe is placed next to the RPA and both probes are moved to centerline when measurements are collected. In this work we hold the downstream distance of the probe fixed at 50 cm. We sweep the bias of the probe from -50 V to 150 V and measure current using a Keithley 2400 SourceMeter. We show an example of a Langmuir probe trace in Fig. 20 To process the data, we begin by subtracting off the ion current following best practices from Lobbia and Beal [18]. We then use three different techniques to find the plasma potential from our Langmuir probe traces. The first is based on the first derivative of our I-V trace, where we plot $\frac{dI}{dV}$ as a function of bias voltage and search for the maximum. The second technique is based on the second derivative, where we plot $\frac{d^2I}{dV^2}$ and find the first zero crossing. In the third technique, the probe current is plotted in log space and lines are fit to the ion saturation and electron saturation portions of the trace. The plasma potential is then taken to be the voltage where these two linear fits intersect. This analysis results in three values of plasma potential per probe trace. Repeating this on all three probe traces then yields nine estimates of plasma potential per operating condition. We take the average and standard deviation of these nine values and propagate those values through to our other probe measurements.

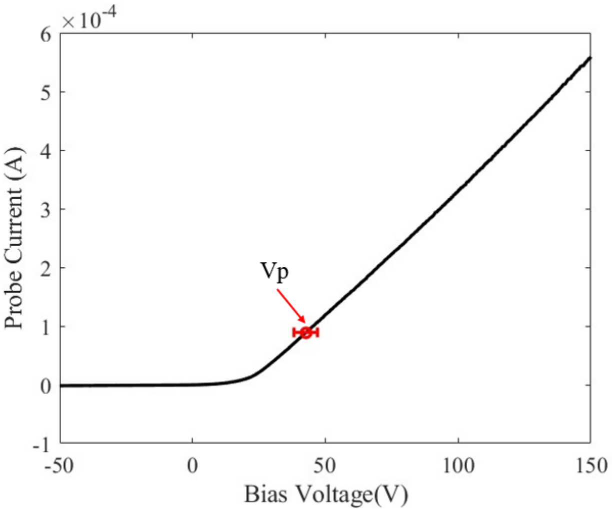

Fig. 20 Sample Langmuir probe trace with plasma potential identified.

2. Retarding Potential Analyzer

The retarding potential analyzer (RPA) uses a series of grids to selectively repel species of the plasma. Here, we employ a three-grid RPA. The first grid is left floating to minimize perturbations to the plasma. The second grid, the electron repelling grid, is biased to a large negative value. For our experiments, we hold the bias of the electron repelling grid constant at -285 V, which is applied using a Gwinstek GPR-30H10D DC power supply. Compared to other EP devices, this electron repelling voltage is far larger in magnitude [28]. For traces taken with lower magnitude repelling potentials, the RPA trace ends negative, indicating electrons are reaching the collector. Therefore, this large repelling potential is necessary to completely repel the high energy electrons of the ECR thruster [12]. The third grid, the ion retarding grid, is biased positive to repel ions. By sweeping the voltage on this grid from 0 V to a large positive potential, we are able to determine the ion energy distribution function (IEDF) in the far field plume. We use a Sorensen DCS 600-1.7E power supply to sweep the ion retarding potential. Simultaneously, voltage is measured across a 10 kΩ shunt, which is connected to the collector of the RPA. Maximum retarding potential was varied depending on the thruster operating condition, but in all tests the bias was sufficiently high to eliminate all ion current to the collector. We show an example RPA trace in Fig. 21, where the probe bias voltage has been corrected for far-field plasma potential. The raw RPA data represents current to the probe collector as a function of bias voltage on the ion retarding grid. Taking the first

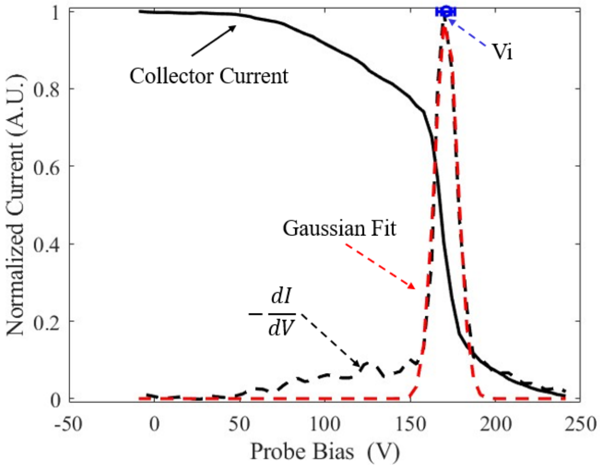

Fig. 21 Sample RPA trace with IEDF and Gaussian fit shown

derivative and multiplying by -1, we are able to determine the IEDF, $IEDF \approx \frac{-dI}{dV}$. Commonly, a Gaussian function is fit to the IEDF and the most probable ion energy is taken to be the mean of this Gaussian. For most of the RPA traces collected in this experimental campaign, the Gaussian fit technique showed good agreement with the derivative based IEDF. However, at some higher power operating conditions, the IEDF became sufficiently broad that the most probable ion energy determined from the Gaussian fit was erroneously low. In these cases, the algorithm was adjusted and the most probable ion energy was taken to be the voltage where the I-V derivative amplitude is maximized. As with the Langmuir probe, the three RPA traces were each analyzed to extract the most probable ion energy, as well as the the uncertainty arising from the IEDF fitting method. Finally, because we correct the RPA traces for plasma potential from the Langmuir probe, we include the uncertainty from our plasma potential measurements in our ion energy analysis.

3. Faraday Probe

Historically, Faraday probes have been the most difficult far-field diagnostic to apply to ECR thrusters [8, 11, 21]. Similar to the electron repelling grid of the RPA, large negative potentials are required to keep the Faraday probe in the ion saturation regime. In this work, we hold the bias voltage constant at -300 V, which is supplied using a Sorensen DCS600-1.7E. The probe is placed 30 cm downstream of the thruster and traversed across the thruster plume using a rotation stage. During the sweep, voltage is measured across a 10 kΩ shunt resistor and recorded by a BK precision 5491B DMM. As with the other probes, we take multiple sweeps of the Faraday probe across the thruster plume.

One major source of uncertainty for Faraday probes is the presence of charge exchange (CEX) ions [17, 29]. Charge exchange collisions occur when a high energy ion collides with a slow neutral and the two particles exchange an electron. These collisions result in a slow moving ion and a fast moving neutral, which can alter the spatially resolved ion current distribution measured by our Faraday probe. In particular, CEX causes residual current in the so called ”wings” of the probe trace, beyond the region where we expect ions from the main thruster plume. The rate of these CEX collisions depends on background pressure in the facility. However, owing to the large probe bias required to characterize ECR thrusters, the probe current resulting from CEX is thought to be significant. Indeed, previous comparisons of global and diagnostic-based performance metrics have found that probes typically over predict thrust and efficiency. This disagreement was largely attributed to overestimation of ion current from the Faraday probe [8, 11, 21]. Because the Faraday probe provides information about ion current for all three efficiency modes, any error propagates through the entire efficiency mode analysis.

The most common method of correcting for erroneous CEX current is to employ a subtraction method to the wings of the probe trace [17]. In this work, we use two different techniques and analyze the traces using each method. The first method is known as "flat subtraction”. This method simply subtracts the residual ion current at 90° from the entire probe trace. While this treatment does recover the expected behavior of zero beam current at 90° to the thruster exit, it also assumes the CEX profile is constant everywhere. To counter this assumption, as a second subtraction method, we fit a Gaussian function to the Faraday probe trace. This also causes current at 90° to reach zero, but does not assume a uniform CEX current profile. We perform these corrections for each probe trace and calculate the ion current based on each subtraction method. Repeating this process for multiple probe traces provide us with a mean and standard deviation for ion current and beam divergence, which are used in our uncertainty analysis.

The final complication with our Faraday probing efforts is probe arcing. Unlike the electron repelling grid of the RPA, which has a floating attenuation grid to minimize thruster perturbations, the plasma plume is directly exposed to the electron repelling potential of the Faraday probe. In our experiments, this caused arcing on the face of the probe. These arcs were often transient and were more frequent at low power operating conditions, particularly for the connected electrical configuration. We suspect that this dependence between arcing and thruster operating condition is linked to the mass utilization of the device and the resulting neutral density. At low operating powers, mass utilization efficiency of the thruster is low, resulting in higher neutral densities in the near-field plume. This increase in local pressure causes arcing to occur more frequently. Typically these arcs were transient and resulted in a single, erroneously high current value. To correct for this effect, we implement an arc detection algorithm, that searches for transient peaks in the Faraday probe trace and replaces them with the local mean of the ion current value. We show a picture of this correction in Fig. 22. Although this algorithm successfully removes the large transient arcs, it does struggle with the smaller, consecutive arcs at large angles. Because the calculation of total ion current is weighed as a function of angle, the residual current content at oblique angles to the thruster likely still causes an overestimate of ion beam current. Examining the efficiency mode analysis presented in Fig. 8, we see this reflected as large uncertainty in our mass utilization measurements at low power and slight overestimation of our total efficiency. Fortunately, as power to the thruster increased, arcing became less problematic, yielding the unprocessed probe traces shown in Fig. 7 at 30 W.

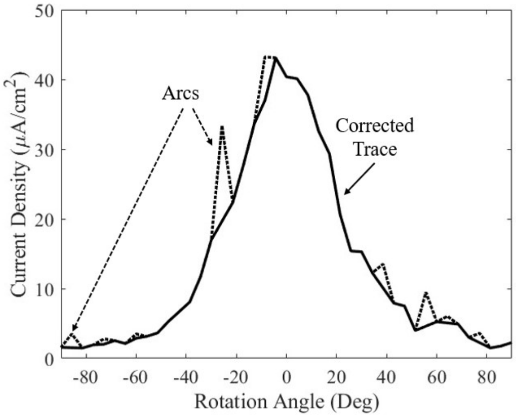

Fig. 22 Faraday Probe trace taken at 20 W, 1 SCCM in the connected electrical configuration. The raw trace is shown as dashed lines, with the trace corrected for arcs in solid black.

4. E × B Probe

The E × B probe is used to determine the charge fractions of the thruster plume. This probe uses a perpendicular electric and magnetic field to filter ions based on their charge. By sweeping the voltage between two parallel plates, we are able to control the strength of the electric field and selectively accept charge populations to the collector of the probe. Following the analysis technique described by Ref. [19], we fit a Gaussian function to each charge population. Integrating each respective function and comparing their integrated currents yields the charge fractions of ion populations in the plume. This analysis technique is shown in Fig. 23. As with the other probe measurements, we take multiple traces of the E × B probe and determine the charge fractions for each. The ion current collected by the Faraday probe is then corrected according to

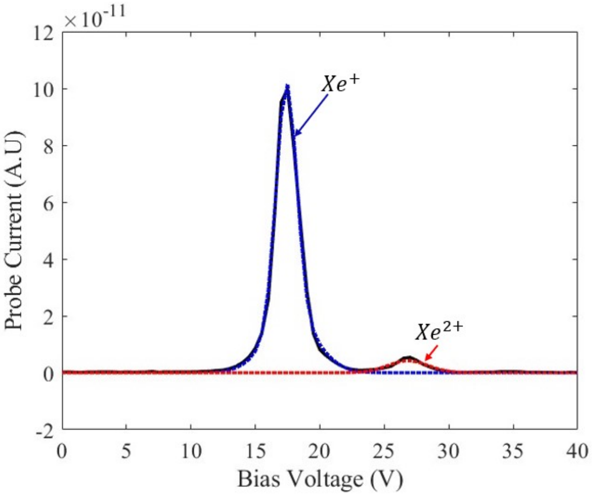

Fig. 23 Gaussian fit processing method for ExB data taken at 20 W in the connected thruster configuration.

$$I_i = I \sum_n \frac{\Omega_n}{qZ_n}. \tag{12}$$

Here I is the current value measured by the Faraday probe, Ω_n is the charge fraction of species n, Z_n is the charge state of species n, and q is the fundamental charge.

References

[1] Jarrige, J., Elias, P.-Q., Cannat, F., and Packan, D., "Performance Comparison if an ECR Plasma Thruster using Argon and Xenon as Propellant Gas," *33rd International Electric Propulsion Conference*, 2013.

[2] Jarrige, J., and et al., "Characterization of a Coaxial ECR Plasma Thruster," *AIAA Space Conference and Exposition*, Vol. 2628, 2013.

[3] Takahashi, K., "Magnetic nozzle radiofrequency plasma thruster approaching twenty percent thruster efficiency," *Scientific Reports*, 2021.

[4] Wachs, B. N., "Optimization and Characterization of Facility Effects for a Low Power Electron Cyclotron Resonance Magnetic Nozzle Thruster," Ph.D. thesis, University of Michigan, 2022.

[5] Sheppard, A. J., and Little, J. M., "Performance Analysis of an Electron Cyclotron Resonance Thruster with Various Propellants," *Journal of Propulsion and Power*, Vol. 38, No. 6, 2022, pp. 998–1007. https://doi.org/10.2514/1.B38698.

[6] Staab, D., Frey, A., Garbayo, A., Shadbolt, L., Andrea, L. F., Gurciullo, A., and Grondein, P., "AQUAJET: an Electrodeless ECR Water Thruster," *Space Propulsion Conference*, 2018.

[7] Désangles, V., Peterschmitt, S., Packan, D., and Jarrige, J., "ECRA thruster advances, 30W and 200W prototypes latest performances," *37th International Electric Propulsion Conference*, Electric Rocket Propulsion Society, 2022.

[8] Vialis, T., Jarrige, J., Packan, D., and Aanesland, A., "Direct Thrust Measurement of an Electron Cyclotron Resonance Plasma Thruster," *Journal of Propulsion and Power*, 2018.

[9] Eckhaus, A. J., and Jorns, B. A., "A Model-Driven Investigation into the Role of Wall Secondary Electron Emission in an Electron Cyclotron Resonance Magnetic Nozzle Thruster," *38th International Electric Propulsion Conference*, Electric Rocket Propulsion Society, 2024.

[10] Eckhaus, A., and Jorns, B., "Experimental Investigation of Wall Material Effects in Electron Cyclotron Resonance Thrusters," *39th International Electric Propulsion Conference*, 2025.

[11] Peterschmitt, S., "Development of a Stable and Efficient Electron Cyclotron Resonance Thruster with Magnetic Nozzle," Ph.D. thesis, Institut Polytechnique De Paris, 2020.

[12] Hitchens, O., "Performance Increase of Electron Cyclotron Resonance Magnetic Nozzle Thruster via Magnetically Thickened Resonance Region," Ph.D. thesis, University of Surrey, 2025.

[13] Boni, F., Desangles, V., Elias, P.-Q., Jarrige, J., and Packan, D., "Investigation of facility effects on the performance of an electron cyclotron resonance magnetic nozzle thruster," *38th International Electric Propulsion Conference*, 2024.

[14] Goebel, D. M., and Katz, I., *Fundamentals of Electric Propulsion: Ion and Hall Thrusters*, JPL Space Science and Technology Series, 2008.

[15] Chen, F. F., *Introduction to Plasma Physics and Controlled Fusion*, Springer International Publishing, 2016.

[16] Drentje, A., Wolters, U., Nadzeyka, A., Meyer, D., and Wiesemann, K., "Simon short circuit effect in ECRIS," *Review of Scientific Instruments*, Vol. 73, No. 2, 2002, pp. 516–520. https://doi.org/10.1063/1.1429315.

[17] Brown, D. L., Walker, M., Szabo, J., Huang, W., and Foster, J., "Recommended Practice for Use of Faraday Probes in Electric Propulsion Testing," *Journal of Propulsion and Power*, Vol. 33, No. 3, 2017.

[18] Lobbia, R. B., and Beal, B. E., "Recommended Practice for Use of Langmuir Probes in ElectricPropulsion Testing," *Journal of Propulsion and Power*, Vol. 33, 2017.

[19] Huang, W., and Shastry, R., "Analysis of Wien filter spectra from Hall thruster plumes," *Review of Scientific Instruments*, 2015.

[20] Lemmer, K., "Recommended Practices for Design and Use of Retarding Potential Analyzers in Electric Propulsion," *39th International Electric Propulsion Conference*, 2025.

[21] Pioch, R., Desangles, V., and Chabert, P., "Investigation of the directional Faraday cup and improvement of the comparison between direct and indirect thrust measurements of a magnetic nozzle ECR thruster," *Physics of Plasmas*, 2024.

[22] Sanchez-Villar, A., Boni, F., Desangles, V., Jarrige, J., Packan, D., Ahedo, E., and Merino, M., "Comparison of a hybrid model and experimental measurements for a dielectric-coated coaxial ECR thruster," *Plasma Sources Science and Technology*, 2023.

[23] Lafleur, T., “Helicon Plasma Thruster Discharge Model,” *Physics of Plasmas*, Vol. 21, 2014. https://doi.org/10.1063/1.4871727.

[24] Lafleur, T., Packan, D., Cannat, F., Jarrige, J., and Elias, P.-Q., “Modelling of magnetic nozzle thrusters with application to ECR and Helicon thrusters,” Vol. 359, 2015. https://doi.org/https://electricrocket.org/IEPC/IEPC-2015-359_ISTS-2015-b-359.pdf.

[25] Correyero, S., Jarrige, J., Packan, D., and Ahedo, E., “Plasma beam characterization along the magnetic nozzle of an ECR thruster,” *Plasma Sources Science and Technology*, Vol. 28, 2019.

[26] Jarrige, J., Correyero, S., Elias, P. Q., and Packan, D., “Investigation on the ion velocity distribution in the magnetic nozzle of an ECR plasma thruster using LIF measurements,” *35th International Electric Propulsion Conference*, 2017].

[27] Wachs, B. N., and Jorns, B. A., “Sub-millinewtwon thrust stand and wireless power coupler for microwave-powered small satellite thrusters,” *Review of Scientific Instruments*, 2022.

[28] Su, L. L., Roberts, P. J., Gill, T. M., Hurley, W. J., Marks, T. A., Sercel, C. L., Whittaker, M. G. A. C. B., Viges, E., and Jorns, B. A., “High-Current Density Performance of a Magnetically Shielded Hall Thruster,” *Journal of Propulsion and Power*, 2024. https://doi.org//10.2514/1.B39324.

[29] Huang, W., Shastry, R., Soulas, G. C., and Kamhawi, H., “Farfield Plume Measurement and Analysis on the NASA-300M,” Tech. rep., NASA, 2013.